Lightweight AlCuFeMnMgTi High Entropy Alloy with High Strength-to-Density Ratio Processed by Powder Metallurgy

Myoung Jin Chae[1,2] · Ashutosh Sharma[1,2] · Min Chul Oh[3] · Byungmin Ahn[1,2]

Abstract

In this study, we synthesized a new $Al_{16.6}Cu_{16.6}Fe_{16.6}Mn_{16.6}Mg_{16.6}Ti_{16.6}$ lightweight high entropy alloy (LWHEA) by high energy ball milling and spark plasma sintering (SPS). The effect of milling time (15, 30, 45, and 60 h) and SPS conditions (600 and 700 °C) on microstructure, hardness, and density of LWHEAs were studied. The results showed that milled LWHEA is base centered cubic (BCC) structured, consisting of dual BCC1/BCC2 matrix with dispersed minor Cu_2Mg precipitates and Ti. After SPS of milled samples, the BCC2 phase fraction was increased gradually. The distribution of Ti was uniform up to 45 h milled sample SPSed at 600 °C. However, porosity was built up beyond 45 h milling and higher SPS temperature (700 °C). The presence of finer secondary phases in the HEA matrix contributes to the dispersion hardening. The optimum microhardness and density of LWHEA AlCuFeMnMgTi were around 770 HV and 4.34 g cm^{-3} which is superior to other conventional alloys such as Al or Ti-based alloys.

Keywords High entropy alloy · Lightweight · Powder metallurgy · Spark plasma sintering · Microstructure

1 Introduction

Unlike the traditional engineering alloys, such as Fe–C, Al–4Cu or Sn–37Pb alloys containing a single principal element, multi-principal element alloys are being studied continuously. These novel multi-element alloys are termed as high entropy alloys which contain 5 or more elements in 5–35 at% compositions [1]. Each one of the principal elements has been shown to directly affect the physical and chemical properties of the material, such as the crystal structure, melting point, density, and show novel properties. High entropy alloy discovery by Yeh et al. and Cantor et al. in 2004 proved that a high configurational entropy stabilizes the solid solution and restricts the growth of brittle and hard phases [2, 3]. According to B. Cantor, the total number of possible high entropy alloy systems can be as high as 10^{177} for almost sixty different combinations of elemental composition differing by 0.1% [1, 4]. Various permutations and combinations have already been tried and studied to design a lightweight high entropy alloy (LWHEA) where the density is lesser or nearly 7 g cm^3. Several researchers have contributed to the development of LWHEA in the past [5–8]. For instance, Youssef et al. fabricated an $Al_{20}Li_{20}Mg_{10}Sc_{20}Ti_{30}$ LWHEA by milling at subzero temperatures and obtained face-centered cubic (FCC) structure which transformed into a hexagonal close-packed (HCP) structure after the conventional sintering process. Their study showed a minimum density of 2.67 g cm^{-3} [9]. In another work by Tseng et al. $Al_{20}Be_{20}Fe_{10}Si_{15}Ti_{35}$ LWHEA was produced by melting and casting approach and obtained high hardness (~ 911 HV) and a density of 3.91 g cm^{-3} [10]. Raman et al. produced CrMoNbTiW HEA via powder metallurgy with a high hardness of 8.9 GPa [11]. However, for demanding applications, even higher strength and/or plasticity are required from the application point of view. Therefore, often researchers have exploited various mechanisms like precipitation hardening, dispersion strengthening, twinning, nanostructuring or metastability to tailor the LWHEA properties [12–15].

Myoung Jin Chae and Ashutosh Sharma have contributed equally to this work.

✉ Byungmin Ahn
  byungmin@ajou.ac.kr

1 Department of Materials Science and Engineering, Ajou University, Suwon 16499, Republic of Korea

2 Department of Energy Systems Research, Ajou University, Suwon 16499, Republic of Korea

3 Metals Forming Technology R&D Group, Korea Institute of Industrial Technology, Incheon 21999, Republic of Korea

Most of the high entropy alloys are concentrated on the composition of Cantor elements (Co, Cr, and Ni) for phase stabilization. However, these elements are heavy and are not suitable for the weight reduction of high entropy alloys. Also, the addition of all these elements makes the final product extremely expensive. Among, existing LWHEAs, popular elements such as Al, Mg, and Ti, have been selectively added into high entropy alloy through arc melting process. Various other elements have been explored for LWHEA like Li, V, Si, Sc, Zn, etc. to achieve excess weight reduction [6]. However, few of these elements (V, Li) may cause toxic effects on humans as well as are expensive. Silicon is good for LWHEA development, but it has a diamond cubic structure and may need modification of Si particles while Zn is usually avoided due to its low vapor pressure point which requires special handling procedures [6].

Conventionally produced high entropy alloys by arc melting and casting involve repeated melting and solidification, which produce fragile microstructures, build segregation and dendrites in the microstructure [16, 17]. Novel deformation processes have been utilized to improve the final microstructure, e.g., mechanical alloying and high-pressure torsion [17, 18]. Furthermore, additional steps are to be introduced for eliminating these casting defects. Among other methods, the manufacturing of LWHEA using advanced powder metallurgy is an attractive and superior method that can provide improved microstructure. In particular, the production of LWHEA through HEBM and SPS is a low-temperature process, relatively easy in composition control, and has the advantage of controlling the microstructure through the HEBM approach [19–21]. Besides, even if the difference in the melting point of each element is large, it has the advantage of manufacturing an alloy successfully [18, 22]. In one study, powder metallurgy processed HEAs have been shown to have more than 80% flexural strength as compared to cast counterpart [23].

In the present investigation, we produced a new LWHEA consisting of Al, Cu, Fe, Mn, Mg, and Ti. We used an advanced powder metallurgy approach for the alloy fabrication and overcome the problems related to conventional casting or sintering as seen in most of the previously reported high entropy alloys. We studied the effect of HEBM and SPS temperature conditions to obtain an optimized set of microhardness and strength per unit density. Finally, we compared the mechanical strength of AlCuFeMnMgTi alloy with the other important engineering materials. The mechanical alloying was achieved by HEBM and bulk samples were prepared by the densification of alloy powder via SPS. The alloying behavior and microstructure of LWHEAs were studied concerning milling and SPS conditions.

2 Experimental Method

The equiatomic AlCuFeMnMgTi alloy was chosen to produce LWHEA. All the elemental powders are procured from the Sigma Aldrich, USA. The thermodynamic criteria for high entropy effect, mixing entropy (ΔS_{mix}), valence electron concentration (VEC), atomic size difference (δ), and density are shown in Table 1 [1, 5].

The HEBM processss was applied for mechanical alloying of powder mixture in a planetary milling machine (RETSCH PM400, Germany). The ratio of the stainless steel ball and the powder was 10:1. The powder mixture was charged into stainless steel milling vessel, revolving at 300 rpm in an argon atmosphere. We milled the powder mixture for 15, 30, 45, and 60 h. Subsequently, 12 g of the prepared powder was placed in a graphite mold having a diameter of 20 mm and then compacted and SPSed in sintering equipment (Dr. Sinter Lab, Japan). The sintering was done at various sintering temperatures (600, 700 °C for 10 min, 100 °C/min) at a load of 30 MPa in Ar atmosphere. We fixed the SPS temperature according to the change in Z-axis punch displacement with sintering time. There was a slight change in the slope of Z-axis displacement below 600 °C. The specimen shrinkage occurred from 600–700 °C. Therefore, we fixed SPS temperatures at 600 °C and 700 °C. We discarded further experiments at SPS temperature of 800 °C due to melting of Al and Mg components.

The phase analysis of powder and sintered specimens was investigated using an X-ray diffractometer (XRD, Rigaku Miniflex 200, Japan). The samples were scanned in Cu-Kα radiation in the range of 2θ angle from 20° to 80° at 2°/min. We used step scan mode using the Rigaku JADE 6.5 XRD analysis software. The powder crystallite size of various phases is calculated by Scherer equation given by:

$$D_v = \frac{0.89\lambda}{\beta cos\theta} \tag{1}$$

where D_v is the average crystallite size and β is the full width at half maximum of the peak.

To observe the microstructure of the alloyed powder and sintered body, scanning electron microscopy (SEM, JSM IT500HR, JEOL, Japan) was sued. The compositional analysis was done using energy-dispersive X-ray spectroscopy (EDS) detector of the SEM machine. The 60 h samples were used for bulk HEA characterization and property evaluation.

Table 1 Thermodynamic parameters of the LWHEA studied

Composition	ΔS_{mix} (J/mol/K)	δ (%)	VEC	D (g cm^{-3})
$Al_{16.6}Cu_{16.6}Fe_{16.6}Mn_{16.6}Mg_{16.6}Ti_{16.6}$	14.89	5.38	5.83	4.47

The theoretical density (D_{theory}) of the LWHEA was determined by the rule of mixtures according to the equation,

$$D_{theory} = \frac{\sum x_j M_j}{\sum x_j M_j / D_j} \qquad (2)$$

where x_j, D_j, and M_j are the atomic fraction, density and atomic mass of the ith element. The experimental density was estimated by the Archimedes principle.

The mechanical strength of the SPSed compacts was determined by a Vickers microhardness tester (Mitutoyo HM-200, Japan). The applied load and time were 100 gf and 10 s, respectively. The measurements were performed at 20 random locations and the average value is reported.

3 Result and Discussion

3.1 Phase Evolution of Powder and Bulk LWHEA

Figure 1 shows the XRD patterns of powder AlCuFeMnMgTi LWHEA obtained at different milling times and SPS temperatures. We can see from the XRD patterns that the LWHEA is a body-centered cubic (BCC) structured. The major peaks are attributed to BCC1, BCC2, Cu_2Mg, and Ti (Fig. 1a). The formation of Cu_2Mg was noticed which can be due to the interdiffusion of Cu/Mg pair to form an intermetallic compound (IMC) Cu_2Mg with milling time [24]. It appears that Cu_2Mg phase hardly decreases and remains in the matrix even after 45 or 60 h of milling. BCC1 and BCC2 phases are formed at all milling times, and BCC2 phase showed a tendency to increase with milling time (Fig. 1b). Also, the Ti peak was found to decrease with an increase in HEBM time. The alloying of Ti is was not achieved even after milling for 60 h. Besides, the refinement of the Ti particles and their dispersion in the matrix at higher milling times was noticed.

The reason can be due to the highest melting point of Ti among all the constituents. This is because elements with a low melting point have a higher diffusion coefficient in the solid-state [25–27]. It is, therefore, judged that the order of alloying of the constituent elements is related to the melting point of the constituent elements. After milling for 30 h, the intensity of BCC2 phase is increased gradually. With the increase of milling time, the peak broadening is also verified as shown by Fig. 1b. The powder crystallite size calculated from the main peak by the Scherer Eq. (1), is shown in Table 2.

It can be seen that the crystallite size of BCC1/BCC2 phases decreases rapidly with an increase in HEBM time. BCC1 is the major phase in this alloy at initial stages of milling while BCC2 phase increases with milling time and an equal ratio of BCC1/BCC2 is obtained after 60 h. The BCC2 phase is slightly finer as compared to BCC1 (Table 2). As the BCC2 phase fraction increases, the size of BCC1 phase is slightly decreased with milling time due to the increase in grain size strengthening effect [28].

Figure 2a, b displays the XRD patterns of the bulk LWHEA after densification at 600 and 700 °C. The various phases include BCC1/BCC2, Cu_2Mg and Ti. It can be seen that the ratio of BCC2/BCC1 phases increased after SPS. We already mentioned that the ratio of BCC1 and BCC2 phase was almost similar in 60 h milled LWHEA. The Cu_2Mg phase is present at 42.3° after 15 h milling at 600 and 700 °C.

However, the Cu_2Mg phase at 42.3° was depressed after 30 and 45 h. This is because of the increase of milling energy with milling time. The Cu_2Mg peaks become slightly less intense when sintering temperature is raised to 700 °C. It indicates that a high sintering temperature causes evaporation of Mg from the LWHEA and a fraction of Cu_2Mg phase decreases. It is reported that after heating of the Cu/Mg diffusion pair above 200 °C, initially, the first phase forms is $CuMg_2$ phase. However, when the temperature exceeds 400 °C, the presence of copper atoms surrounding Mg gives rise to Cu_2Mg [24].

Furthermore, in all cases, the fraction of BCC2 phase always increases in sintered compacts produced at higher milling times. Also, Ti is present only as a single entity in the XRD pattern of sintered samples. It may be possible that due to the HCP structure and high melting point of Ti (highest in this study), its alloying behavior is different than other phases having a BCC structure. Recently, Alcala et al. [29], has reported that the segregation and alloying behavior of the high entropy alloys are directly related to the melting temperature of the constituents, which also supports the present observations.

3.2 Microstructure of Bulk LWHEA

Figure 3 shows the morphology of the bulk AlCuFeMnMgTi LWHEA SPSed at different temperatures. The microstructure shows various light gray and bright phases. As discussed previously, based on XRD of powder and SPSed samples, AlCuFeMnMgTi LWHEA consists of BCC1 and BCC2. The two different regions in the microstructure correspond to BCC1 in the white color followed by BCC2 in gray color. The bigger flakes type dark particles, present at initial stages of milled samples (15 and 30 h) are Ti particles. The size of dark Ti particles also gets reduced after increased HEBM time.

The black spots in the circle indicate the pores present in the consolidated samples which are higher in the sample SPSed at 700 °C (60 h). Also, the Cu_2Mg phase was found to be in an atomic ratio of 2:1 at higher 700 °C. The presence of Cu_2Mg precipitates is also supported by EDS and XRD
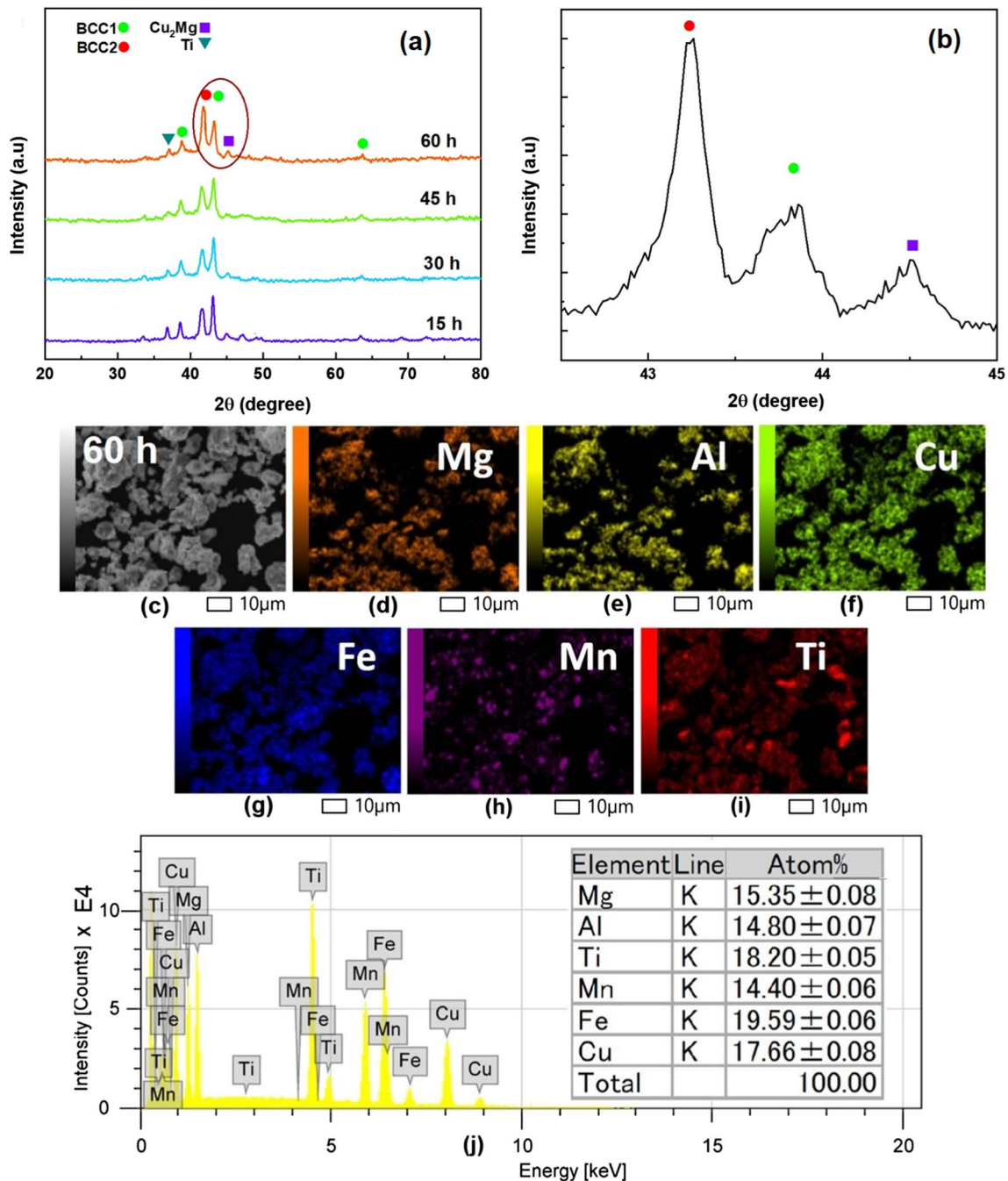
Fig. 1 **a** XRD patterns of 15, 30, 45, and 60 h HEBMed AlCuFeMnMgTi LWHEA, **b** enlarged view of XRD pattern of HEA HEBMed for 60 h, **c** SEM image of 60 h HEBMed alloy, **d–i** EDS elemental maps obtained from **c**, and **j** EDS spectrum of 60 h HEBMed alloy

Table 2 The powder crystallite size of BCC1/BCC2 phases after different milling times

Milling time (h)	Crystallite size (nm)	
	BCC1	BCC2
15	28	35
30	25	26
45	19	20
60	17	19

results. The EDS compositional analysis of each phases was done to ensure the composition of various phases.

Table 3 shows that important phases formed in the AlCuFeMnMgTi LWHEA are Cu-rich BCC (CuMgAl), Fe-rich BCC (FeMnTi) and Cu_2Mg phase. The analysis of various phases by EDS confirms a FeMnTi-rich BCC (BCC1) in the bright region while a CuMgAl-rich BCC (BCC2) is present in the dark areas. The EDS mapping
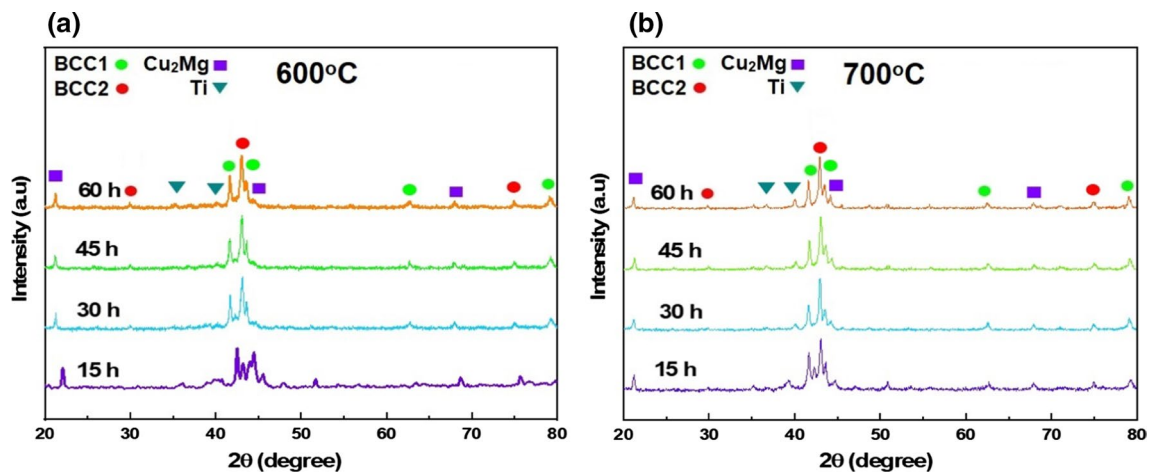
Fig. 2 XRD patterns of SPSed AlCuFeMnMgTi LWHEA (60 h) at **a** 600 and **b** 700 °C
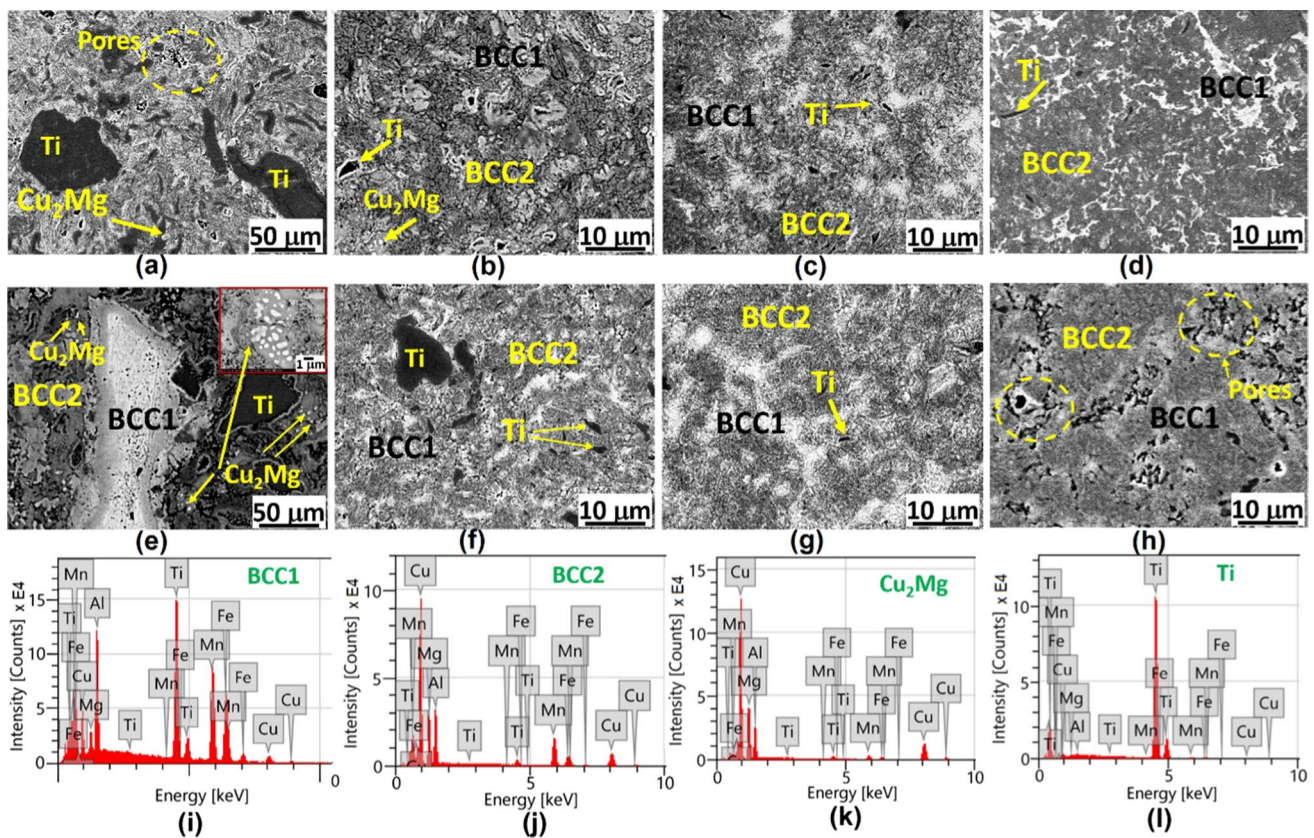

Fig. 3 SEM images of the AlCuFeMnMgTi bulk sample milled for various times and consolidated at various SPS temperature. **a** 15 h, 600 °C, **b** 30 h, 600 °C, **c** 45 h, 600 °C, **d** 60 h, 600 °C, **e** 15 h, 700 °C, **f** 30 h, 700 °C, **g** 45 h, 700 °C, **h** 60 h, 700 °C, and **i–l** EDS analysis of the various peaks shown in 700 °C, 15 h

of every element of HEA SPSed at 600 °C is shown in Fig. 4. The presence of scattered Ti particles is confirmed which are dispersed in the LWHEA matrix (shown by encircled areas, Fig. 4g, o). Ti is present as the dispersed phase rather than alloyed phase embedded in the matrix.

Also, the Ti-particle size reduces from $70 - 0.8$ μm after increasing milling times up to 60 h.

Besides, the densification of the 60 h milled sample at 700 °C showed a lot of porosities in the microstructure. This is confirmed from the EDS mapping every element of HEA

**Table 3** EDS compositional analysis of various phases in AlCuFeMnMgTi LWHEA

Process condition	Phase	EDS composition (at%)					
		Al	Cu	Fe	Mn	Mg	Ti
600 °C, 15 h	BCC1	29.25	5.71	22.24	18.09	4.47	20.24
	BCC2	18.58	27.8	7.83	24.01	19.15	2.63
	Precipitate	15.59	45.88	2.99	4.71	28.69	2.14
600 °C, 30 h	BCC1	25.65	16.61	17.99	15.43	5.85	18.47
	BCC2	13.81	49.06	1.88	3.47	30.33	1.45
	Precipitate	13.61	48.55	3.00	5.17	26.88	2.79
600 °C, 45 h	BCC1	20.16	11.06	21.05	18.07	9.23	20.43
	BCC2	20.68	28.90	4.64	20.41	3.05	22.32
	Precipitate	11.74	49.25	4.15	6.06	24.33	4.47
600 °C, 60 h	BCC1	21.57	14.09	16.09	18.05	10.99	19.21
	BCC2	15.80	26.86	14.22	12.03	18.28	12.81
	Precipitate	14.93	21.59	15.69	16.85	14.27	16.67
700 °C, 15 h	BCC1	21.82	10.31	20.99	22.59	7.03	17.26
	BCC2	13.99	50.89	2.58	5.20	26.65	0.69
	Precipitate	4.37	62.46	2.60	2.02	27.56	0.99
700 °C, 30 h	BCC1	12.91	17.73	18.90	19.61	17.48	13.37
	BCC2	22.88	29.90	22.30	2.53	2.21	20.18
	Precipitate	13.49	44.52	3.65	7.32	26.01	5.01
700 °C, 45 h	BCC1	21.54	16.42	12.07	20.68	9.18	20.11
	BCC2	22.23	27.57	22.31	3.56	13.40	10.93
	Precipitate	14.33	47.73	2.13	4.49	29.73	1.59
700 °C, 60 h	BCC1	24.21	16.05	20.85	19.56	9.53	9.80
	BCC2	19.92	28.55	23.37	8.83	16.31	3.02
	Precipitate	14.32	25.03	15.62	18.55	6.92	19.56

Fig. 4 SEM-EDS elemental maps of AlCuFeMnMgTi consolidated samples at 600 °C. **a** SEM image, **b**–**g** Elemental maps, **h** EDS analysis of sample produced at 60 h and 600 °C
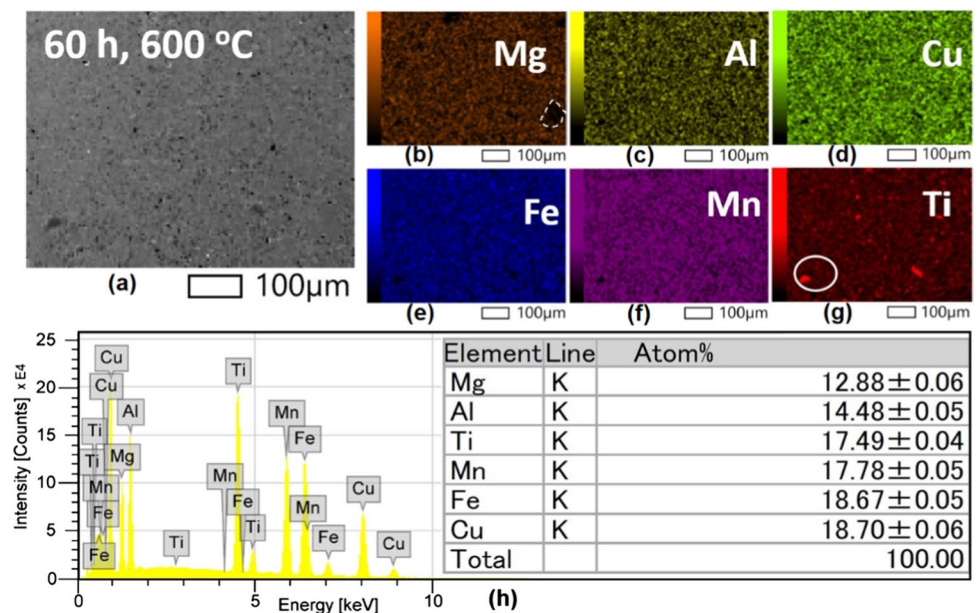
SPSed at 700 °C is shown in Fig. 5. The introduction of porosity may be attributed to the heavy loss of Mg as noticed after comparing Figs. 4b, h and 5b, h. The loss of Mg content is higher at SPS temperature 700 °C, though there is

Fig. 5 SEM-EDS elemental maps of AlCuFeMnMgTi consolidated samples at 700 °C. **a** SEM image, **b**–**g** elemental maps, **h** EDS analysis of sample produced at 60 h and 700 °C
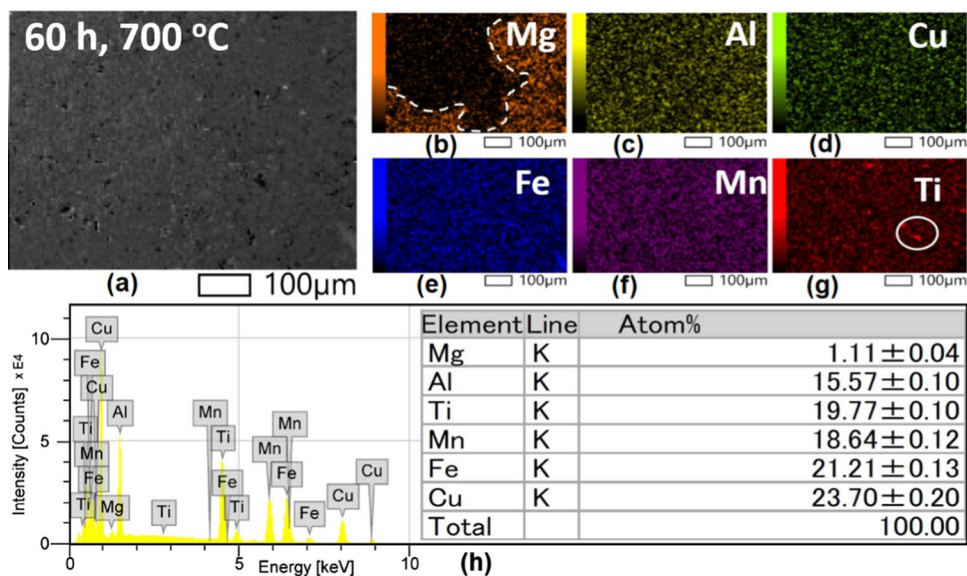
no big change in the size of Ti particles with the increase in SPS temperature.

3.3 Microhardness and Density

The microhardness of samples milled for various times and sintered at various temperatures is shown in Fig. 6. The hardness of SPSed samples milled for higher times is higher. The hardness increases as 685 HV (6.71 GPa), 710 HV (6.96 GPa), and 750 HV (7.35 GPa) for SPSed samples milled for 15, 30 and 45 h, respectively. The maximum microhardness of the SPS sample was 770 ± 12 HV (7.55 ± 0.12 GPa) obtained at 60 h, 600 °C. We also presented the indentation marks after measuring hardness for the 60 h milled sample.

As the HEBM time increases up to 30 h, the hardness value increases considerably which is higher at higher SPS temperature. For example, the hardness varies as 695 HV (6.81 GPa), 735 HV (7.20 GPa), 745 HV (7.30 GPa) for

SPSed samples milled for 15, 30 and 45 h, respectively. This is due to the presence of Ti and Cu_2Mg precipitates which assist in the hardening of the HEA matrix. However, the hardness value of the sample (60 h) SPSed at 700 °C decreases slightly to 712HV (6.98 GPa). The reason can be related to the presence of porosity at higher SPS temperature and milling time as observed in the SEM micrographs (Fig. 3h).

After comparing the indentation marks for both cases (60 h, 600 °C; 60 h, 700 °C), it was found that few minor cracks were formed in sample fabricated at 60 h of HEBM and SPSed at 600 °C, while numerous cracks were noticed for sample fabricated at 60 h of HEBM and SPSed at 700 °C. This means that the sample processed at 60 h, 700 °C has a slightly lower microhardness as compared to the sample processed at 60 h, 600 °C. Finer size of BCC2 and BCC1 also contribute to the overall hardening of the HEA (Table 2) leading to higher microhardness. However, the reason for the

Fig. 6 **a** Microhardness of the LWHEA as a function of HEBM time and SPS temperature, and **b** Indentation impression obtained after microhardness tests
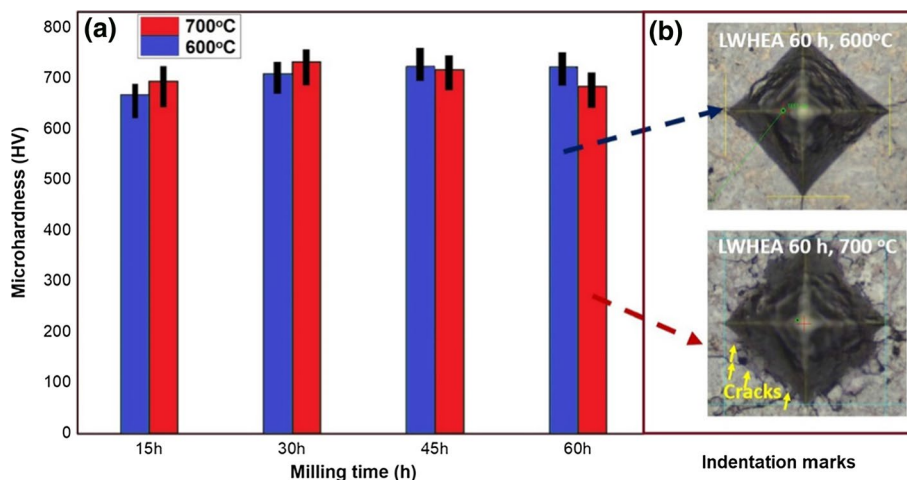
difference in hardness is due to the precipitated Cu_2Mg and Ti phases that contribute to the dispersion hardening in addition to the grain size strengthening at higher 60 h, 700 °C. From the XRD results (Fig. 1), higher milling times leads to an increase in the fraction of BCC2 phase as compared to the BCC1 phase. The BCC1 and BCC2 phase fraction remains almost similar at 60 h.

However, a different trend was observed after SPS treatment of HEAs. The volume fraction of BCC1 becomes smaller than BCC2 phase (Fig. 2). The volume fraction of BCC2 increases while volume fraction of BCC1 phase decreases. An increase in BCC2 phase fraction enhances the formation of Cu_2Mg particles in the BCC2 matrix as observed from the well-defined peaks of Cu_2Mg in XRD results (Fig. 2). Higher SPS temperature resulted in the higher volume fraction of brittle Cu_2Mg particles with fine spherical structure in the BCC2 matrix as shown by the XRD and SEM results (Figs. 2, 3). The hardness value thus improves with increase in Cu_2Mg phase in samples processed up to 45 h and 700 °C. However, increased segregation of Cu_2Mg and Ti particles might result in pore formation and lowering of microhardness, in samples processed

beyond 45 h, 700 °C. A similar observation was also noticed by Dong et al. and Zhou et al. where fine precipitates were found to enhance the strengthening mechanisms of the HEA [30, 31]. Therefore, the enhancement of the microhardness of the alloy is attributed to the presence of BCC1 and BCC2 phases and precipitation strengthening of HEA matrix by secondary Cu_2Mg and Ti particles. The numerous cracks indicate the presence of hard but porous microstructure which may have generated during Mg loss in the microstructure as noticed by SEM studies.

The measured Archimedes density of the LWHEA is summarized in Table 4. The density of the LWHEA lies in the range of 4.11–4.34 g cm^{-3}. Initially (15 h), the density was around 4.11–4.13 g cm^{-3} corresponding to 93% of theoretical density. This can be expected due to lower sintering temperature (600 °C) and poor densification. The maximum density was achieved for 60 h milled samples and SPSed at 600 °C which corresponds to almost 97% of theoretical density. The density variation is lesser in samples milled up to 45 h irrespective of SPS temperatures. However, there is a drastic decrease in density for the 60 h sample SPSed at 700 °C. This study suggests a build-up of porosity in the sample SPSed at 700 °C. Therefore, the HEBM time and SPS temperatures for this alloy should be around 45 h and 600 °C for better realization of lightweight properties.

3.4 Strength and Density

The comparison of the strength and density of AlCuFeMnMgTi with other alloys processed by powder metallurgy route is given in Fig. 7. We choose the sample 60 h and
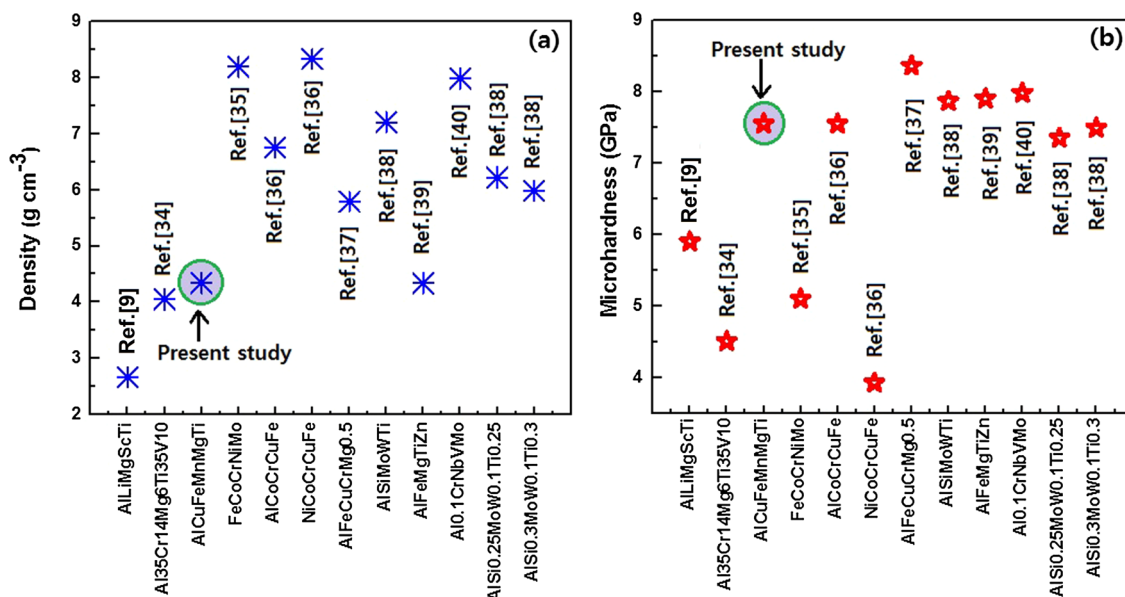
Table 4 Density of the LWHEA at various milling times and SPS temperature

Milling time (h)	Density (g cm^{-3})	
	600 °C	700 °C
15	4.11	4.13
30	4.20	4.28
45	4.31	4.30
60	4.34	4.19

Fig. 7 Comparison of **a** density and **b** microhardness of powder metallurgy processed HEAs [9, 33–40].

SPSed at 600 °C due to its superior sintered density and hardness. The theoretical strength per unit density of this sample is ~ 563 MPa g cm^{-3} [32].

It can be seen that our produced AlCuFeMnMgTi LWHEA shows a comparable hardness in comparison to most of the HEAs processed by powder metallurgy route (Fig. 7a). The density of most of the HEAs are shown in Fig. 7b. Additionally, the density of the present LWHEA is almost 50% lesser as compared to high strength Inconel 718 (8.19 g cm^{-3}), and similar to popular Ti6Al4V (~ 4.43 g cm^{-3}) alloy. Our manufactured LWHEA does not contain toxic or expensive elements, such as V, Li, Be, Cr or Zn unlike others [8–10, 34]. It means our LWHEA promises an economical way to produce LWHEA by an advanced powder metallurgy route. We also compared the results of our work with existing powder metallurgy based LWHEA as shown in Fig. 7. It can be seen that the data obtained in our work is consistent with the others and is even better or comparable to the existing lightweight Al or Ti alloys produced via powder metallurgy route.

4 Conclusions

We designed and produced a new LWHEA AlCuFeMnMgTi successfully by an advanced powder metallurgy route with a low density of 4.34 g cm^3. We used HEBM for 60 h followed by the densification by SPS method. The results showed that 60 h HEBMed powder had a BCC1/BCC2 structure. However, after the SPS, the proportion of BCC2 increases and becomes prominent. This tendency also improves at higher SPS temperatures (700 °C). Longer milling times increased BCC2 phase fraction while higher SPS temperature increased the formation of Cu$_2$Mg phases and porosity. The theoretical density of LWHEA is improved with SPS and is maximum at 600 °C. Higher SPS at 700 °C results in only 93% theoretical density while a lower SPS 600 °C results in 97% density due to the loss of Mg at 700 °C. The strength to weight ratio is around 563 MPa cm^3 g^{-1} calculated from the microhardness (770 HV) and density 4.34 g cm^{-3}. This study shows that the specific strength of the alloy produced in the present study can be a potential candidate for upcoming lightweight and strong alloys.

References

1. B.S. Murty, J.W. Yeh, S. Ranganathan, *High-Entropy Alloys*, 1st edn. (Elsevier, Butterworth-Heinemann, 2014), pp. 1–218
2. B. Cantor, I.T.H. Chang, P. Knight, A.J.B. Vincent, Mater. Sci. Eng. A **375–377**, 213 (2004)
3. J.W. Yeh, S.K. Chen, S.J. Lin, J.Y. Gan, T.S. Chin, T.T. Shun, C.H. Tsau, S.Y. Chang, Adv. Eng. Mater. **6**, 299 (2004)
4. B. Cantor, Entropy **16**, 4749 (2014)
5. Y. Zhang, T.T. Zuo, Z. Tang, M.C. Gao, K.A. Dahmen, P.K. Liaw, Z.P. Lu, Prog. Mater. Sci. **61**, 1 (2014)
6. A. Kumar, M. Gupta, Metals **6**(9), 199 (2016)
7. X. Huang, J. Miao, A.A. Luo, J. Mater. Sci. **54**, 2271 (2019)
8. N.D. Stepanov, N.Y. Yurchenko, E.S. Panina, M.A. Tikhonovsky, S.V. Zherebtsov, Mater. Lett. **188**, 162 (2017)
9. K.M. Youssef, A.J. Zaddach, C. Niu, D.L. Irving, C.C. Koch, Mater. Res. Lett. **3**, 95 (2014)
10. K. Tseng, Y. Yang, C. Juan, T. Chin, C. Tsai, J. Yeh, Sci. China Technol. Sci. **61**, 184 (2018)
11. L. Raman, K. Guruvidyathri, G. Kumari, S.V.S.N. Murty, R.S. Kottada, B.S. Murty, J. Mater. Res. **34**, 756 (2019)
12. J.Y. He, H. Wang, H.L. Huang, X.D. Xu, M.W. Chen, Y. Wu, X.J. Liu, T.G. Nieh, K. An, Z.P. Lu, Acta Mater. **102**, 187 (2016)
13. Y. Deng, C.C. Tasan, K.G. Pradeep, H. Springer, A. Kostka, D. Raabe, Acta Mater. **94**, 124 (2015)
14. S.S. Nene, M. Frank, K. Liu, R.S. Mishra, B.A. McWilliams, K.C. Cho, Sci. Rep. **8**, 9920 (2018)
15. Y. Zou, J.M. Wheeler, H. Ma, P. Okle, R. Spolenak, Nano Lett. **17**, 1569 (2017)
16. J.M. Sanchez, I. Vicario, J. Albizuri, T. Guraya, E.M. Acuña, Sci. Rep. **9**, 6792 (2019)
17. F. Lukáč, M. Dudr, J. Čížek, P. Harcuba, T. Vlasák, M. Janeček, J. Kuriplach, J. Moon, H.S. Kim, J. Zýka, J. Málek, Acta Phys. Pol. A **134**, 891 (2018)
18. S. Mridha, S. Samal, P.Y. Khan, K. Biswas, Govind, Metall. Mater. Trans. A **44**, 4532 (2013)
19. S. Nam, S.E. Shin, J.H. Kim, Met. Mater. Int. (2020). https://doi.org/10.1007/s12540-020-00769-8
20. W. Wang, B. Li, S. Zhai, J. Xu, Z. Niu, J. Xu, Y. Wang, Met. Mater. Int. **24**, 1112 (2018)
21. Y.A. Alshataif, S. Sivasankaran, F.A. Al-Mufadi, A.S. Alaboodi, H.R. Ammar, Met. Mater. Int. **26**, 1099 (2020)
22. J.M. Torralba, P. Alvaredo, A.G. Junceda, Powder Metall. **62**(2), 84 (2019)
23. L.M. Gouvea, I. Moravcik, M. Omasta, J. Veselý, J. Cizek, P. Minárik, J. Cupera, A. Záděra, V. Jan, I. Dlouhy, Mater. Charact. **159**, 110046 (2020)
24. A.Y. Volkov, A.A. Kalonov, D.A. Komkova, A.V. Glukhov, Phys. Met. Metallogr. **119**, 946 (2018)
25. Y.E. Lee, S.L. Houser, *Essential Readings in Light Metals* (Springer, Cham, 2016), pp. 44–50
26. S. Hori, H. Tai, E. Matsumoto, J. Jpn. Inst. Light Met. **34**(7), 377 (1987)
27. J. Lin, M. Huang, W. Yang, L. Xing, Sci. Rep. **8**, 15190 (2018)
28. Y. Song, M. Wang, Y. Zong, R. He, J. Jin, Materials **11**, 1903 (2018)
29. M.D. Alcala, C. Real, I. Fombella, I. Trigo, J.M. Cordoba, J. Alloys Compd. **749**, 834 (2018)
30. Y. Dong, Y. Lu, J. Kong, J. Zhang, T. Li, J. Alloys Compd. **573**, 96 (2013)
31. Y.J. Zhou, Y. Zhang, Y.L. Wang, G.L. Chen, Appl. Phys. Lett. **90**, 181904 (2007)
32. G.E. Dieter, Mechanical Metallurgy, *SI Metric Edn* (McGraw-Hill Book Company, London, 1988), pp. 282–295
33. C.C. Juan, J.W. Yeh, T.S. Chin, A novel light high-entropy alloy Al$_{20}$Be$_{20}$Fe$_{10}$Si$_{15}$Ti$_{35}$, E-MRS Fall Meeting, Symposium I, Warsaw, Poland, (2009)
34. P. Chauhan, S. Yebaji, V.N. Nadakuduru, T. Shanmugasundaram, J. Alloys Compd. **820**, 153367 (2020)

35. M. Zhang, W. Zhang, Y. Liu, B. Liu, J. Wang, Powder Met. **61**(2), 123 (2018)
36. S. Praveen, B.S. Murty, R.S. Kottada, Mater. Sci. Eng. A **534**, 83 (2012)
37. O. Maulik, D. Kumar, S. Kumar, D.M. Fabijanic, V. Kumar, Intermetalics **77**, 46 (2016)
38. L.R. Kanyane, A.P.I. Popoola, N. Malatji, P.N. Sibisi, Mater. Today Proc. (2020). https://doi.org/10.1016/j.matpr.2020.02.095
39. B. Kang, J. Lee, H.J. Ryu, S.H. Hong, J. Alloys Compd. **767**, 1012 (2018)
40. V.H. Hammond, M.A. Atwater, K.A. Darling, H.Q. Nguyen, L.J. Kecskes, JOM **66**, 2021 (2014)